The Astrophysical Journal, 800:69 (10pp), 2015 February 10 doi:10.1088/0004-637X/800/1/69

HIGH-LYING OH ABSORPTION, [C II] DEFICITS, AND EXTREME L_{FIR}/M_{H2} RATIOS IN GALAXIES

E. González-Alfonso[1], J. Fischer[2], E. Sturm[3], J. Graciá-Carpio[3], S. Veilleux[4], M. Meléndez[4], D. Lutz[3], A. Poglitsch[3], S. Aalto[5], N. Falstad[5], H. W. W. Spoon[6], D. Farrah[7], A. Blasco[1], C. Henkel[8,9], A. Contursi[3], A. Verma[10], M. Spaans[11], H. A. Smith[12], M. L. N. Ashby[12], S. Hailey-Dunsheath[13], S. García-Burillo[14], J. Martín-Pintado[15], P. van der Werf[16], R. Meijerink[16], and R. Genzel[3]

[1] Universidad de Alcalá, Departamento de Física y Matemáticas, Campus Universitario, E-28871 Alcalá de Henares, Madrid, Spain
[2] Naval Research Laboratory, Remote Sensing Division, 4555 Overlook Avenue SW, Washington, DC 20375, USA
[3] Max-Planck-Institute for Extraterrestrial Physics (MPE), Giessenbachstraße 1, D-85748 Garching, Germany
[4] Department of Astronomy, University of Maryland, College Park, MD 20742, USA
[5] Department of Earth and Space Sciences, Chalmers University of Technology, Onsala Space Observatory, SE-43992 Onsala, Sweden
[6] Cornell University, Astronomy Department, Ithaca, NY 14853, USA
[7] Department of Physics, Virginia Tech, Blacksburg, VA 24061, USA
[8] Max-Planck-Institut für Radioastronomie, Auf dem Hügel 69, D-53121, Bonn, Germany
[9] Astronomy Department, Kind Abdulaziz University, P.O. Box 80203, Jeddah 21589, Saudi Arabia
[10] University of Oxford, Oxford Astrophysics, Denys Wilkinson Building, Keble Road, Oxford OX1 3RH, UK
[11] Kapteyn Astronomical Institute, University of Groningen, P.O. Box 800, 9700 AV Groningen, The Netherlands
[12] Harvard-Smithsonian Center for Astrophysics, 60 Garden Street, Cambridge, MA 02138, USA
[13] California Institute of Technology, 1200 East California Boulevard, Pasadena, CA 91125, USA
[14] Observatorio Astronómico Nacional (OAN)-Observatorio de Madrid, Alfonso XII 3, E-28014 Madrid, Spain
[15] CSIC/INTA, Ctra de Torrejón a Ajalvir, km 4, E-28850 Torrejón de Ardoz, Madrid, Spain
[16] Sterrewacht Leiden, Leiden University, P.O. Box 9513, 2300 RA, Leiden, The Netherlands
Received 2014 July 29; accepted 2014 December 14; published 2015 February 10

ABSTRACT

Herschel/PACS observations of 29 local (ultra)luminous infrared galaxies, including both starburst and active galactic nucleus (AGN) dominated sources as diagnosed in the mid-infrared/optical, show that the equivalent width of the absorbing OH 65 μm $\Pi_{3/2}$ $J = 9/2$–$7/2$ line (W_{eq}(OH65)) with lower level energy $E_{low} \approx 300$ K, is anticorrelated with the [C II]158 μm line to far-infrared luminosity ratio, and correlated with the far-infrared luminosity per unit gas mass and with the 60-to-100 μm far-infrared color. While all sources are in the active $L_{IR}/M_{H2} > 50 L_{\odot}/M_{\odot}$ mode as derived from previous CO line studies, the OH65 absorption shows a bimodal distribution with a discontinuity at $L_{FIR}/M_{H2} \approx 100\, L_{\odot}/M_{\odot}$. In the most buried sources, OH65 probes material partially responsible for the silicate 9.7 μm absorption. Combined with observations of the OH 71 μm $\Pi_{1/2}$ $J = 7/2$–$5/2$ doublet ($E_{low} \approx 415$ K), radiative transfer models characterized by the equivalent dust temperature, T_{dust}, and the continuum optical depth at 100 μm, τ_{100}, indicate that strong [C II]158 μm deficits are associated with far-IR thick ($\tau_{100} \gtrsim 0.7$, $N_H \gtrsim 10^{24}$ cm^{-2}), warm ($T_{dust} \gtrsim 60$ K) structures where the OH 65 μm absorption is produced, most likely in circumnuclear disks/tori/cocoons. With their high L_{FIR}/M_{H2} ratios and columns, the presence of these structures is expected to give rise to strong [C II] deficits. W_{eq}(OH65) probes the fraction of infrared luminosity arising from these compact/warm environments, which is $\gtrsim$30%–50% in sources with high W_{eq}(OH65). Sources with high W_{eq}(OH65) have surface densities of both L_{IR} and M_{H2} higher than inferred from the half-light (CO or UV/optical) radius, tracing coherent structures that represent the most buried/active stage of (circum)nuclear starburst-AGN co-evolution.

Key words: galaxies: evolution – galaxies: ISM – infrared: galaxies – line: formation

1. INTRODUCTION

From the first spectroscopic observations of (ultra)luminous infrared galaxies ((U)LIRGs) in the far-infrared (far-IR) domain with the *Infrared Space Observatory* (*ISO*), evidence was found that the strength of fine-structure lines (from both ions and atoms) in emission are generally anticorrelated with the depth and excitation of the molecular lines observed in absorption (Fischer et al. 1999). The most commonly observed line, the fine-structure [C II]157.7 μm transition (hereafter [C II]), tends to exhibit a strong deficit with respect to the far-IR luminosity in ULIRGs relative to less luminous systems (Luhman et al. 1998, 2003). In normal galaxies, the [C II]/FIR luminosity ratio remains nearly constant (0.1%–1%), while it decreases in galaxies with warmer far-IR colors (Malhotra et al. 2001; Díaz-Santos et al. 2013). On the other hand, studies of individual templates (Arp 220 and Mrk 231) indicated that high far-IR radiation densities associated with the nuclear regions of galaxies with [C II] deficits are required to account for the observed high-lying molecular absorption (González-Alfonso et al. 2004, 2008, hereafter G-A08).

The launch of the *Herschel Space Observatory* (Pilbratt et al. 2010) has dramatically improved the sensitivity of these measurements. Observations with the PACS spectrometer (Poglitsch et al. 2010) soon revealed that the observed deficit of [C II] relative to the far-IR emission applies to all far-IR fine-structure lines (Fischer et al. 2010; Farrah et al. 2013; Graciá-Carpio et al. 2011, hereafter G-C11). G-C11 also showed that the deficits are better correlated with L_{FIR}/M_{gas} than with L_{FIR}, while PACS observations of three (U)LIRGs with strong line deficits, NGC 4418, Arp 220, and Mrk 231, showed deep absorption in high-lying molecular lines (González-Alfonso et al. 2012, 2014b, hereafter G-A12 and G-A14). NGC 4418 is a case in point, as it shows the highest [C II] deficit, a moderate $L_{IR} \sim 1.5 \times 10^{11} L_{\odot}$ but a high $L_{FIR}/M_{gas} \approx 400\, L_{\odot}/M_{\odot}$ (G-C11), and the highest-lying H_2O absorption among all galaxies with full FIR spectra (G-A12).

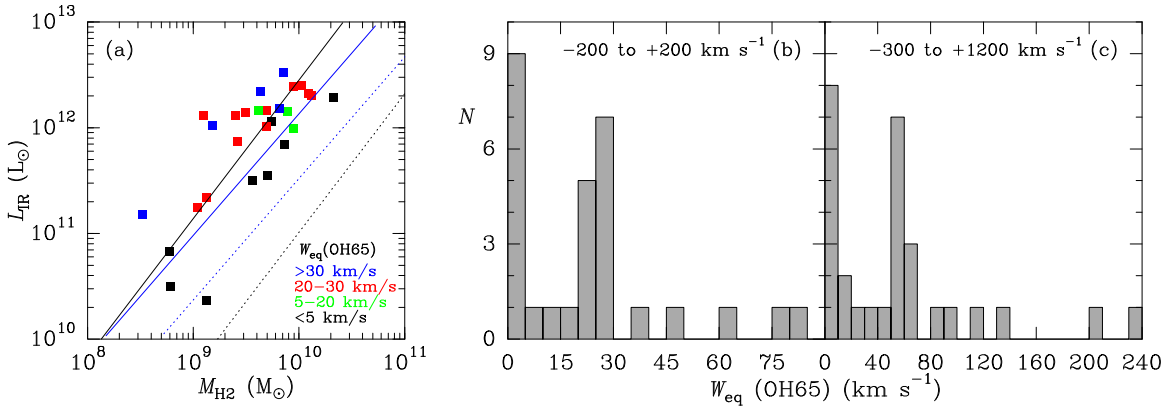

Figure 1. (a) Infrared luminosities as a function of the H_2 masses for our sample of local (U)LIRGs. Symbol colors indicate values of W_{eq}(OH65) in four bins. The solid and dotted lines are fits to ULIRG-SMG-QSO mergers and spiral-BzK-normal galaxies, respectively, given by Daddi et al. (2010, black) and Genzel et al. (2010, blue). (b) Histogram of W_{eq}(OH65) calculated between −200 and +200 km s^{-1} in bins of 5 km s^{-1}, showing an apparent bimodal distribution with a long tail extending up to 85 km s^{-1}. (c) Histogram of W_{eq}(OH65) calculated between −300 and +1200 km s^{-1} (covering essentially the whole doublet), with bins of 10 km s^{-1}.

To explore the connection between intense far-IR fields and both the highly excited molecular gas and the [C II] deficit, we investigate the relationship between the OH $^2\Pi_{3/2}$ J = 9/2–7/2 transition at 65.2 μm (hereafter OH65) with $E_{low} \approx$ 300 K, and the [C II] line, L_{FIR}/M_{gas}, the 9.7 μm silicate absorption, and the far-IR colors, also using measurements of the OH $^2\Pi_{1/2}$ J = 7/2–5/2 transition at 71.2 μm (hereafter OH71, $E_{low} \approx$ 415 K) in galaxies for which it is available. OH is a versatile molecule with high abundances in active regions including photodissociated regions (PDRs), cosmic-ray dominated regions (CRDRs), and X-ray dominated regions (XDRs; e.g., Goicoechea & Cernicharo 2002; Goicoechea et al. 2011; Meijerink et al. 2011; González-Alfonso et al. 2013), and traces powerful galactic-scale molecular outflows in some sources (Fischer et al. 2010; Sturm et al. 2011; Spoon et al. 2013; Veilleux et al. 2013, hereafter V13; G-A14) mostly associated with large active galactic nucleus (AGN) luminosity fractions and luminosities. In extragalactic sources, the OH65 doublet (when detected) is absorption-dominated, indicating that the excitation of the lower $^2\Pi_{3/2}$ J = 7/2 level is governed by radiative (rather than collisional) processes.[17] The OH65 pumping thus involves successive absorptions in the 119, 84, and finally in the 65 μm doublet with high A−Einstein coefficients (0.14, 0.51, and 1.2 s^{-1}, see the energy level diagram of OH in G-A14), thus ensuring an excellent probe of strong far-IR fields.

2. OBSERVATIONS

We have used *Herschel*/PACS observations of the OH65 transition in local ($z < 0.1$) galaxies, included in the *Herschel* guaranteed time key program SHINING (PI: E. Sturm) and in three OT programs (PIs: E. González-Alfonso; J. Fischer; S. Hailey-Dunsheath). Table 1 lists the sample galaxies and their properties. With a total of 29 galaxies, the sample is biased toward ULIRGs (including 17 out of the 18 most luminous sources in the *IRAS* Revised Bright Galaxy Sample; Sanders et al. 2003), but also contains less luminous systems including Seyferts and H II galaxies. The OH71 doublet was observed in a subsample of 15 sources. The locations of the targets in the L_{IR}–M_{H2} plane, shown in Figure 1(a), indicate that all except NGC 4945 (with $L_{IR} = 2.3 \times 10^{10}\,L_\odot$) belong to the high L_{IR}/M_{H2} mode (>50 $L_\odot/M_\odot$) as compared with normal/disk galaxies (Daddi et al. 2010; Genzel et al. 2010).

The data were reduced using the standard PACS reduction and calibration pipeline included in HIPE 6.0 and 10.0, recalibrating the data with a reference telescope spectrum obtained from observations of Neptune (G-C11). A few spectra were also reduced using HIPE 12.0. There are moderate calibration differences (typically ≈10% and in a few sources up to ≈20%) in both line and continuum flux densities between HIPE 6.0 and 10.0–12.0, but the continuum-normalized spectra used to measure the OH equivalent widths were found to be essentially identical in the different versions. Likewise, the PACS-based ratios presented below ([C II]/FIR and $f60/f100$) are not sensitive to global calibration issues.

The OH65 spectra, displayed in Figure 2, are dominated by absorption at central velocities, but some sources show detection of blue wings (e.g., Mrk 231, G-A14). Redshifted reemission by the blue component of the doublet from outflowing gas on the far side of the nucleus has the effect of decreasing the relative strength of the red component of the doublet (see asymmetrical doublets in Figure 2). We measured the equivalent width (W_{eq}) of the OH $\Pi_{3/2}J$ = (9/2) − (7/2) doublet between −200 and +200 km s^{-1} around the blue component of the doublet, and between −300 and +1200 km s^{-1}, covering essentially the whole doublet (Table 2 and Figure 2). This work is focused on the structures traced by the excited OH at central velocities, so hereafter we primarily study W_{eq}(OH65) in the −200 and +200 km s^{-1} velocity range while the outflowing gas component will be treated in a separate study. The OH71 spectra, shown in Figure 3, also indicate peak absorption at central velocities.

Most sources in the sample are unresolved with the PACS 9″ × 9″ spatial resolution, and thus W_{eq}(OH65) measured from the central PACS spaxel applies to the whole galaxy. For resolved sources (M82, Arp 299a, NGC 1068, NGC 253, and NGC 4945), W_{eq}(OH65) was measured from the 25 spaxel combined spectra, covering a field of view (FoV) of 47″ × 47″. Likewise, W_{eq}(OH71), the flux of the [C II] line, the FIR, and the flux densities at 60 and 100 μm ($f60$ and $f100$) were all integrated over the total PACS FoV. Even for the extended sources, the PACS $f60$ and $f100$ agree to within 20% with the 60 and 100 μm *IRAS* flux densities (Sanders et al. 2003; Surace et al. 2004), indicating that PACS recovers the bulk of the galaxy

[17] Collisional excitation of $^2\Pi_{3/2}$ J = 7/2 followed by OH65 absorption is not dominant owing to the high A−Einstein coefficient of the 84 μm ($^2\Pi_{3/2}$ 7/2–5/2) transition; efficient OH65 absorption involves a high radiation density such that it will also dominate the excitation of $^2\Pi_{3/2}$ J = 7/2 under reasonable physical conditions.

Table 1
Sample Galaxies

Galaxy Name	D (Mpc)	L_{IR} (10^{11} $L_\odot$)	L'_{CO} (10^9 L_l)	α_{CO} ($M_\odot/L_l$)	M_{H2} (10^9 $M_\odot$)	L_{FIR}/M_{H2} (10^2 $L_\odot/M_\odot$)	$\tau_{9.7}$	$f25/f60$	$f60/f100$	R_{CO}
(1)	(2)	(3)	(4)	(5)	(6)	(7)	(8)	(9)	(10)	(11)
IRAS 07251-0248	398.0	22.00	5.35	0.803	4.30	4.82	2.62	0.10	1.12	Sp
IRAS 09022-3615	268.0	19.20	26.56	0.803	21.33	0.70	1.10	0.11	0.95	GC
M 82	3.9	0.68	0.75	0.803	0.60	0.79	1.00	0.22	0.94	We05[a]
IRAS 13120-5453	136.0	18.60					1.21	0.07	0.81	
NGC 253	3.3	0.31	0.66	0.929	0.61	0.38	1.10	0.15	0.80	Ho97[b]
NGC 1068	18.0	3.18	4.06	0.896	3.64	0.36	0.30	0.47	0.66	Sc83[c]
IRAS F05189-2524	186.0	13.80	3.90	0.803	3.13	3.20	0.43	0.24	1.23	Pa12
IRAS F08572+3915	261.0	13.20	1.56	0.803	1.25	10.06	3.99	0.24	1.74	So97[d]
UGC 5101	173.0	9.91	5.44	1.650	8.97	0.86	1.68	0.08	0.72	So97[d]
IRAS F10565+2448	193.0	11.40	6.79	0.803	5.45	1.87	0.85	0.09	0.91	So97[d]
Arp 299a	46.5	7.41	3.30	0.803	2.65	1.99		0.20	1.08	Ca99
IRAS F11506-3851	49.0	2.19	1.39	0.954	1.32	1.45		0.06	0.76	Mi90[e]
IRAS F12112+0305	333.0	20.40	16.25	0.803	13.06	1.19	1.41	0.09	0.88	Ch09
NGC 4418	35.9	1.50	0.41	0.803	0.33	3.65	4.04	0.22	1.38	Pa12
Mrk 231	186.0	33.70	8.84	0.803	7.10	3.46	0.65	0.25	1.25	So97[d]
NGC 4945	3.4	0.23	0.48	2.754	1.32	0.14	2.79	0.07	0.50	He94[f]
Mrk 273	166.0	14.50	6.11	0.803	4.91	2.75	1.90	0.10	1.22	So97[d]
IRAS F14348-1447	376.0	20.90	15.23	0.803	12.24	1.72	2.10	0.07	0.94	Ch09
IRAS F14378-3651	304.0	14.60	5.18	0.803	4.16	2.98	1.47	0.10	1.08	Mi90[e]
Zw 049.057	58.0	1.76	0.97	1.116	1.09	1.49		0.04	0.78	Pa12
IRAS F15250+3609	245.0	10.60	1.88	0.803	1.51	5.97	3.30	0.18	1.34	Ch09
Arp 220	79.4	15.20	8.17	0.803	6.56	2.56	2.83	0.06	0.99	So97[d]
NGC 6240	106.0	6.98	9.16	0.803	7.36	0.73	1.52	0.15	0.89	So97[d]
IRAS F17207-0014	187.0	25.00	13.12	0.803	10.54	2.53	1.68	0.04	1.01	Pa12
IRAS F19297-0406	383.0	24.60	11.13	0.803	8.94	2.44	1.43	0.09	0.98	So97[d]
IRAS F20551-4250	185.0	10.20	6.10	0.803	4.90	1.84	2.69	0.14	1.28	Mi90[e]
IRAS F22491-1808	343.0	13.20	3.12	0.803	2.51	5.22	1.23	0.10	1.28	Ch09
NGC 7469	64.5	3.52	2.98	1.697	5.06	0.46	0.07	0.21	0.74	Pa12
IRAS F23365+3604	281.0	14.30	9.61	0.803	7.72	1.59	1.69	0.12	1.01	So97[d]

Notes. Column 1: galaxy name; Column 2: distance to the galaxy; adopting a flat universe with $H_0 = 71$ km s^{-1} Mpc^{-1} and $\Omega_M = 0.27$. For some nearby galaxies alternative distances are used; Column 3: IR luminosity (8–1000 μm), estimated using the fluxes in the four *IRAS* bands (Sanders et al. 2003; Surace et al. 2004); Column 4: CO (1–0) luminosity from previous studies (col 12), L_l = K km s^{-1} pc^2; Column 5: conversion factor, $M_{H2} = \alpha_{CO} \times L'_{CO}$, α_{CO} increases with decreasing $f60/f100$; Column 6: H_2 mass; Column 7: far-IR luminosity (40–500 μm) to H_2 mass ratio; Column 8: apparent optical depth of the silicate absorption at 9.7 μm (Spoon et al. 2007); Column 9: continuum 25-to-60 μm flux density ratio; Column 10: continuum 60-to-100 μm flux density ratio; Column 11: Reference for L'_{CO}. Sp: spoon, unpublished data taken with the IRAM 30 m telescope; GC: Graciá-Carpio, unpublished CO(2–1) data taken with APEX, and assuming $L'_{CO2-1}/L'_{CO1-0} = 0.7$; We05: Weiß et al. (2005); Ho97: Houghton et al. (1997); Sc83: Scoville et al. (1983); Pa12: Papadopoulos et al. (2012); So97: Solomon et al. (1997); Ca99: Casoli et al. (1999); Mi90: Mirabel et al. (1990); Ch09: Chung et al. (2009); He94: Henkel et al. (1994).

[a] CO (1–0) flux within the central 3×3 kpc^2, which reduces to half within the inner 1×1 kpc^2.

[b] Corrected for our adopted distance.

[c] Adopting $S_\nu/T_A^* = 42$ Jy/K for FCRAO (Papadopoulos et al. 2012) and correcting for extended emission.

[d] CO (1–0) fluxes corrected for $S_\nu/T_{MB} = 4.95$ Jy/K, IRAM-30m telescope.

[e] Adopting $S_\nu/T_R^* = 24.5$ Jy/K for SEST.

[f] Corrected for extended emission, a CO (1–0) flux of 1.7×10^4 Jy km s^{-1} is estimated.

far-IR continuum emission and the W_{eq}(OH) represent global values. The *IRAS* 25 μm flux densities ($f25$) are then also used in our analysis. All PACS-measured [C II] line fluxes agree with the *ISO*-LWS values or upper limits (Brauher et al. 2008) within 40%, and most of them within 25%. Most values of M_{H2} were estimated from the spatially integrated CO(1–0) luminosities from previous studies (Table 1) by using a conversion factor α_{CO} decreasing with $f60/f100$ (G-C11). Since the sources in our sample are warm, $\alpha_{CO} = 0.8$ was mostly applied (Table 1); only UGC 5101, NGC 7469, and especially NGC 4945 have significantly higher $\alpha_{CO} > 1.2$.

3. RESULTS

W_{eq}(OH65) shows a bimodal distribution (Figures 1(b)–(c) and 2) with peaks at <5 and 20–30 km s^{-1} and a long tail extending up to 85 km s^{-1}. A Pearson χ^2-test comparing the observed distribution for central velocities in Figure 1(b) with a flat distribution gives a P-value ≈0.01, which remains low (0.03) when the full doublet is considered (Figure 1(c)). While most ULIRGs are strong in OH65, some of them (IRAS 09022-3615, UGC 5101, IRAS F10565+2448) are weak and, conversely, there are three sources with moderate luminosities that are strong in OH65 (NGC 4418, Zw 049.057, and IRAS F11506-3851). Nevertheless, sources with high OH65 absorption have, on average, higher infrared luminosities for *fixed* M_{H2} (Figure 1(a)). Among galaxies with low W_{eq}(OH65) < 10 km s^{-1}, some still have clear detections of OH65 (IRAS F10565+2448, UGC 5101, IRAS 09022-3615, NGC 4945, NGC 253), but no trace of OH65 absorption is found in others (M 82, NGC 1068, NGC 7469). OH71 is detected in the

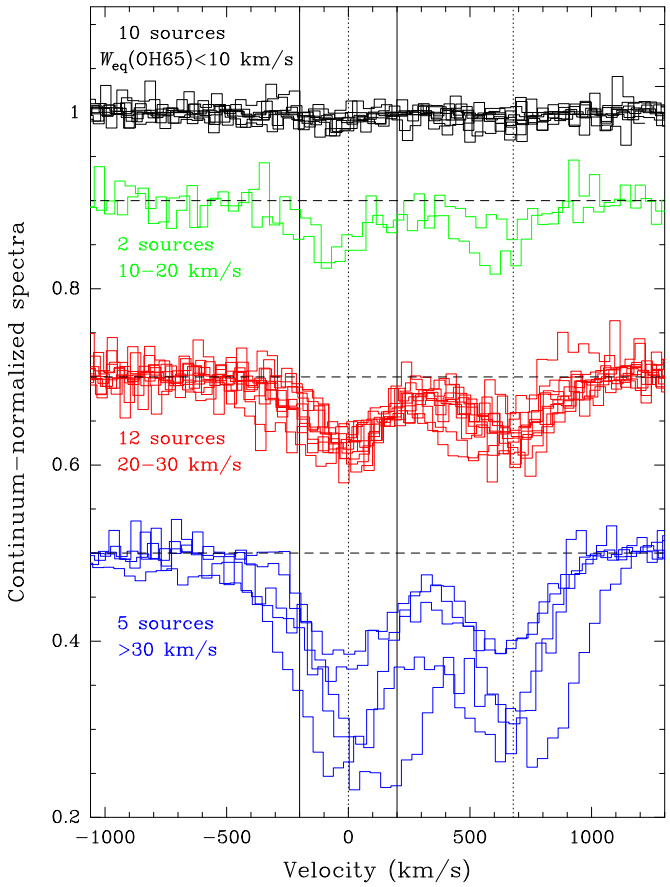

Figure 2. OH $^2\Pi_{3/2}$ 65 μm $J = (9/2) - (7/2)$ continuum-normalized spectra in all galaxies in the sample, with the velocity plotted relative to the rest-frame wavelength of the blue component of the doublet ($J = (9/2^-) - (7/2^+)$ line at 65.1316 μm). The spectra are grouped according to the values of the equivalent width measured between −200 and +200 km s^{-1} around the blue component (indicated by the solid vertical lines and listed in Table 2). The dotted vertical lines indicate the positions of the two components of the doublet. The green, red, and blue spectra are vertically shifted for clarity.

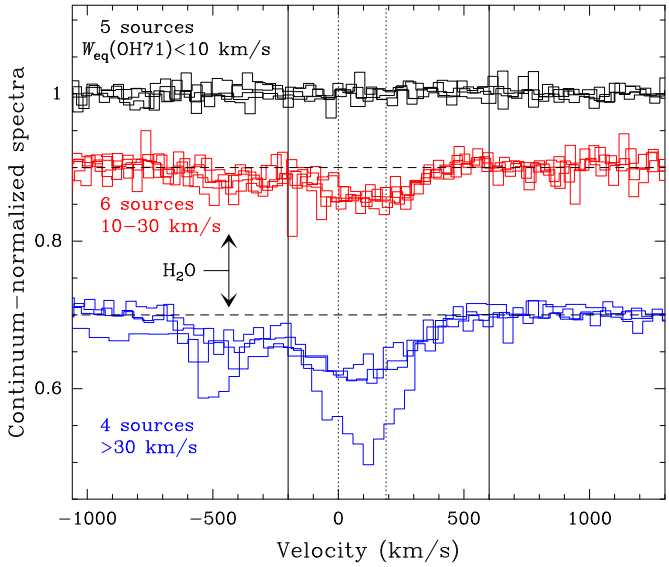

Figure 3. OH $^2\Pi_{1/2}$ 71 μm $J = (7/2) - (5/2)$ continuum-normalized spectra in all 15 galaxies for which it is available, with the velocity plotted relative to the rest-frame wavelength of the blue component of the doublet at 71.171 μm. The dotted vertical lines indicate the positions of the two Λ-components of the doublet, which are blended into a single spectral feature. The spectra are grouped according to the values of the equivalent width measured between −200 and +600 km s^{-1} (indicated by the vertical solid lines and listed in Table 2). The red and blue spectra are vertically shifted for clarity. The position of the H_2O $5_{24} - 4_{13}$ line ($E_{low} \approx 400$ K) is indicated.

10 sources with W_{eq}(OH65) > 20 km s^{-1} (Figure 3, Table 2) and is undetected in the remaining five sources where OH65 is weak or undetected.

Figure 4(a) shows that W_{eq}(OH65) and [C II]/FIR are anticorrelated, with data points mainly concentrated in the upper-left and lower-right quadrants. The [C II]/FIR value that separates the two regimes, $\approx 10^{-3}$, is similar to that found by Luhman et al. (2003) for the onset of the [C II] deficit. Within the limitations of our sample, the data in Figure 4(a) show *that galaxies with a strong [C II] deficit have relatively deep OH65 absorption*. Around the critical value of [C II]/FIR $\sim 10^{-3}$, however, there are galaxies with high and low OH65 absorption. The objects with high W_{eq}(OH65) and also high [C II]/FIR are Arp 299 and IRAS 11506-3851, the former having a complex structure with multiple nuclei[18] and the latter showing the coldest $f60/f100$ color among sources with W_{eq}(OH65) > 10 km s^{-1}. On the other hand, IRAS 13120-5453, NGC 253, IRAS 10565+2448, NGC 4945, and UGC 5101 are examples of galaxies at or close to the onset of the [C II] deficit that lack high OH65 absorption.

Since L_{FIR}/M_{H2} and [C II]/FIR are anticorrelated (G-C11), a positive correlation between the former and W_{eq}(OH65) is anticipated, and this is seen in Figure 4(b). A discontinuity in OH65 absorption is found at $L_{FIR}/M_{H2} \sim 100\, L_\odot/M_\odot$, similar to the one that separates mergers from normal galaxies in the [C II]/FIR–L_{FIR}/M_{gas} plane (G-C11).[19] It is worth noting that M_{H2} is the most uncertain value in Figure 4; however, Figure 5 shows that the correlation remains when using the CO (1–0) luminosity directly, and that [C II]/FIR shows a marked anticorrelation with L_{FIR}/L'_{CO}.

Figure 4(c) relates W_{eq}(OH65) and the apparent optical depth of the 9.7 μm silicate feature (Spoon et al. 2007). With the exception of the nearly edge-on galaxy NGC 4945, sources with weak W_{eq}(OH65) < 10 km s^{-1} have moderate $\tau_{9.7} \lesssim 1.7$, suggesting that a significant fraction of the silicate absorption in the most obscured ($\tau_{9.7} \gtrsim 2$) objects is produced by the material responsible for the OH65 absorption. This is consistent with the finding by Goulding et al. (2012) that the dominant contribution to the silicate feature in Compton-thick AGNs is dust located in the host galaxy, which we identify in part with the OH65 structure.[20] The trends seen in Figures 4(a) and (c) are also consistent with the observed anti-correlation between [C II]/FIR and the strength of the 9.7 μm silicate feature (Díaz-Santos et al. 2013). With increasing silicate obscuration, the low-lying OH 119 μm doublet shows increasing absorption relative to emission, suggesting obscuration of the OH re-emission behind a far-IR optically thick (circum)nuclear region (Spoon et al. 2013, V13); the data suggest that this is also

[18] The FoV was centered in the Arp 299 *A*1−nucleus (IC 694, Aalto et al. 1997) where the peak OH65 absorption is found, but includes extended [C II] and CO emitting regions.

[19] We note that M 82, with a global $L_{FIR}/M_{H2} \sim 80\, L_\odot/M_\odot$, has a CO(1–0) luminosity of half the total value within the PACS FoV (Weiß et al. 2005, see also Table 1), and hence $L_{FIR}/M_{H2} \sim 160\, L_\odot/M_\odot$ in this region. Nevertheless, inhomogeneities are also expected in unresolved sources (Section 4.2 below), and thus we use the global values of M_{H2} in Figure 4(b).

[20] We consider the OH65 region to be part of the host even though it is circumnuclear (see footnote 23), because it is much larger than the pc-scale tori surrounding Compton-thick AGNs. In Arp 220 and NGC 4418, where the [O I] 63 μm line is observed primarily in absorption, a significant fraction of the Si absorption is likely produced in extended regions (G-A12).

Table 2
Herschel/PACS Measurements of W_{eq}(OH65), W_{eq}(OH71), and [C II]/FIR

Galaxy Name (1)	W_{eq}(OH65) (km s^{-1}) (2)	W_{eq}(OH65) (km s^{-1}) (3)	W_{eq}(OH71) (km s^{-1}) (4)	[C II]/FIR (10^{-3}) (5)	ObsID OH65 (6)	ObsID OH71 (7)	ObsID [C II]158 μm (8)
IRAS 07251-0248	79.2(2.7)	200.9(5.4)		0.43	1342207824		1342207825
IRAS 09022-3615	3.9(1.9)	15.3(3.8)		1.79	1342209406		1342209403
M 82	<1.6	<3.5	<2.4	2.08	1342186799	1342186799	1342186798
IRAS 13120-5453	<1.3	<2.5	<2.5	0.78	1342214630	1342248349	1342214629
NGC 253	1.7(0.4)	3.5(0.8)		0.84	1342237602		1342199415
NGC 1068	<2.0	<3.7	<2.6	2.65	1342203128	1342203120	1342191154
IRAS F05189-2524	26.0(1.7)	63.1(3.3)	15.6(3.3)	0.33	1342219445	1342248557	1342219442
IRAS F08572+3915	29.9(6.8)	38.2(12.6)	23.5(3.4)	0.39	1342208954	1342245405	1342208952
UGC 5101	5.5(1.8)	12.7(3.5)		1.03	1342208950		1342208949
IRAS F10565+2448	3.0(1.0)	6.6(1.9)		1.05	1342207790		1342207788
Arp 299a	22.4(1.3)	54.3(2.5)	16.4(2.8)	2.45	1342254241	1342254242	1342208906
IRAS F11506-3851	23.9(1.7)	56.8(3.4)	12.7(3.2)	1.77	1342248551	1342248549	1342248549
IRAS F12112+0305	22.7(3.0)	54.9(6.0)		0.99	1342210833		1342210832
NGC 4418	64.6(1.4)	136.1(2.6)	68.8(1.3)	0.09	1342202115	1342202107	1342210830
Mrk 231	45.2(0.9)	111.7(1.7)	35.8(2.8)	0.36	1342207782	1342253534	1342186811
NGC 4945	3.2(0.5)	7.5(0.9)		0.98	1342247790		1342212221
Mrk 273	27.3(1.3)	81.8(2.5)	37.1(2.1)	0.82	1342207803	1342257292	1342207802
IRAS F14348-1447	29.9(1.0)	69.9(2.0)		0.94	1342224244		1342224242
IRAS F14378-3651	13.9(2.2)	22.5(4.4)		0.46	1342204339		1342204338
Zw 049.057	25.8(2.2)	63.5(4.2)	16.9(2.3)	0.46	1342248366	1342248365	1342248365
IRAS F15250+3609	84.5(2.7)	238.5(5.0)		0.42	1342213754		1342211825
Arp 220	38.4(1.0)	93.4(2.0)	40.5(1.5)	0.22	1342238937	1342238928	1342191306
NGC 6240	4.2(1.9)	<6.8	<5.2	3.86	1342216624	1342251372	1342216623
IRAS F17207-0014	22.2(0.7)	55.0(1.4)	17.4(2.2)	0.58	1342229694	1342252279	1342229693
IRAS F19297-0406	20.2(2.7)	45.4(5.1)		0.83	1342208893		1342208891
IRAS F20551-4250	26.1(1.3)	56.1(2.6)		1.01	1342208936		1342208934
IRAS F22491-1808	26.0(3.3)	53.9(6.2)		0.74	1342211826		1342211825
NGC 7469	<3.4	<6.6	<6.7	2.30	1342235674	1342235841	1342211171
IRAS F23365+3604	17.9(1.6)	50.6(3.1)		0.60	1342212517		1342212515

Notes. Column 1: galaxy name; Column 2: equivalent width of OH65 between −200 and +200 km s^{-1} around the blue component of the doublet, covering the central velocity component; Column 3: equivalent width of OH65 between −300 and +1200 km s^{-1}, around the blue component of the doublet, covering the whole doublet; Column 4: equivalent width of OH71 between −200 and +600 km s^{-1}, covering the whole doublet. Numbers in parenthesis indicate 1σ uncertainties and upper limits are 2σ. These σ values are calculated as $\sigma_{\rm rms}^{\rm norm} \times \Delta V/n^{1/2}$, where $\sigma_{\rm rms}^{\rm norm}$ is the RMS noise of the continuum-normalized spectrum and ΔV and n are the velocity coverage and number of channels over which W_{eq}(OH65) is measured; Column 5: [C II] to FIR (42.5–122.5 μm, following Helou et al. 1988) flux ratio; Column 6: identification number for the OH65 observations; Column 7: identification number for the OH71 observations; Column 8: identification number for the [C II] 158 μm observations.

accompanied by high OH excitation as measured by the high-lying OH65 doublet. High OH65 absorption, however, does not guarantee deep silicate absorption, as seen for a number of sources including the Seyferts Mrk 231 and IRAS F05189-2524.

Figures 4(d) and (e) shows no apparent correlation between W_{eq}(OH65) and $f25/f60$, but shows a positive correlation with the $f60/f100$ far-IR color. In light of the anti-correlation between W_{eq}(OH65) and [C II]/FIR (Figure 4(a)), this is consistent with the decline observed in [C II]/FIR with warmer far-IR colors (Malhotra et al. 2001; Luhman et al. 2003; Díaz-Santos et al. 2013). While $f60/f100 > 1$ is associated with the structure traced by the OH65 absorption, there is a vertical overlap of sources showing strong and weak OH65 absorption within the $f60/f100 \lesssim 1$ bin. Finally, no relationship is found between W_{eq}(OH65) and either the optical spectral type or the fractional contribution of the AGN to the bolometric luminosity as diagnosed from $f15/f30$ (method 6 in Veilleux et al. 2009, hereafter V09).

4. RADIATIVE TRANSFER MODELS

To characterize the overall physical conditions derived from the present observations, and to interpret the trends shown in Figure 4, phenomenological radiative transfer models have been generated (G-A14 and references therein). The model sources are spherical and assume uniform physical conditions, parameterized by the dust temperature ($T_{\rm dust}$), the continuum optical depth at 100 μm (τ_{100}), the gas temperature and density ($T_{\rm gas}$ and $n_{\rm H}$), the OH and C^+ column densities ($N_{\rm OH}$ and N_{C^+}), and the velocity dispersion (ΔV).

4.1. Single-component Models

Initially, we naively assume that the OH65 absorption and [C II] emission arise from the same region and that the covering factor of the continuum by the excited OH is unity; these assumptions represent only a first approach to the interpretation of the observations but still enable us to extract some general conclusions. To decrease the number of free parameters, we approximate some of them according to previous chemical or radiative transfer models. (1) The gas column density ($N_{\rm H}$) is directly related to τ_{100} by adopting a standard gas-to-dust ratio by mass of 100 and a dust mass opacity coefficient at 100 μm of $\kappa_{100} = 44.5\,{\rm cm^2\ g^{-1}}$: $N_{\rm H} = 1.3 \times 10^{24}\,\tau_{100}\,{\rm cm^{-2}}$ (González-Alfonso et al. 2014a). (2) $N_{\rm OH}$ is fixed by assuming an OH abundance relative to H of 2.5×10^{-6} (G-A12,

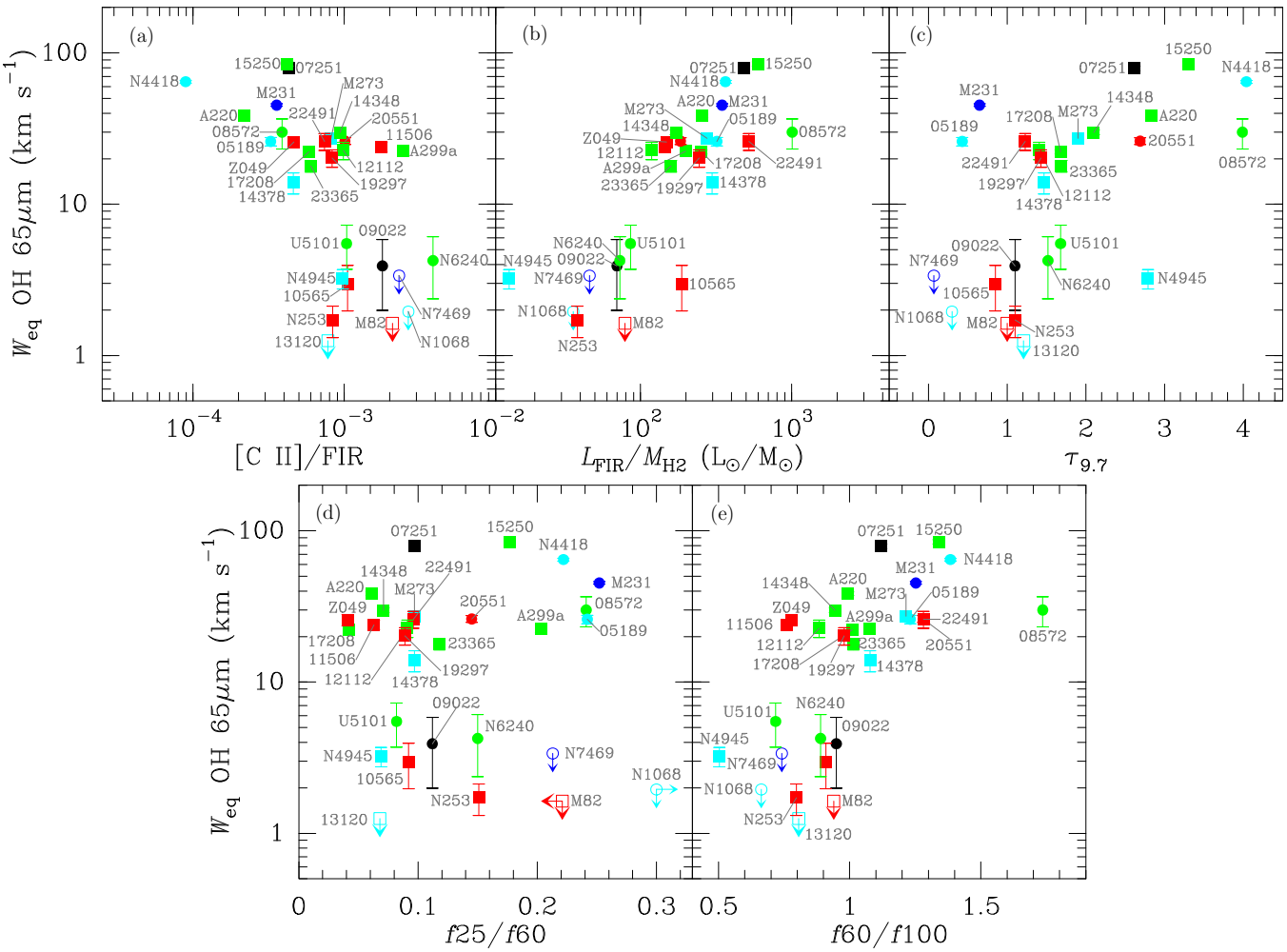

Figure 4. Equivalent width of the OH $\Pi_{3/2}$ $J = (9/2^-) - (7/2^+)$ line at 65.132 μm (the blue component of the 65 μm doublet) between −200 and +200 km s^{-1}, as a function of (a) the [C II]158 μm line to FIR ratio, (b) the far-IR luminosity per unit gas mass, (c) the apparent optical depth of the silicate absorption at 9.7 μm (from Spoon et al. 2007), (d) the 25-to-60 μm color, and (e) the 60-to-100 μm color. Abbreviated source names are indicated. Red, green, blue, light-blue, and black colors indicate H II, LINER, Seyfert-1, Seyfert-2, and unclassified optical spectral types, respectively (from Veilleux et al. 1995, 1999; Véron-Cetty & Véron 2006; Rupke et al. 2005; García-Marín et al. 2006; Kim et al. 1998; V09, or NED/SIMBAD). Circles and squares indicate sources with fractional AGN contribution to the bolometric luminosity of $\alpha_{AGN} \geqslant 50\%$ and <50%, respectively, as derived from $f15/f30$ (V09). Pearson χ^2 independence-tests give chance probabilities $P = 0.012$–0.0–0.043–0.74–0.025 for panels (a)–(e), respectively.

G-A14). (3) We assume that the [C II] emission is dominated by PDRs (Farrah et al. 2013) and N_{C^+} is estimated on the basis of previous models (e.g., Abel et al. 2009; Kaufman et al. 1999, G-C11). For a single PDR, $N_{C^+} \sim 10^{18}$ cm^{-2} is typically inferred for high incident far-UV radiation intensity G_0, and $T_{dust} \sim 10 \times G_0^{0.2}$ K characterizes the warm dust in PDRs (Hollenbach et al. 1991). We set $X_{C^+} = (2\text{–}6) \times 10^{-5}$ for $T_{dust} =$ 30–90 K to approximately account for these results and calculate N_{C^+} based on $N_H(\tau_{100})$. (4) We adopt $n_H = 5 \times 10^4$ cm^{-3} and $T_{gas} = 150$ K, i.e., high density conditions appropriate for the circumnuclear regions of (U)LIRGs, ensuring that the [C II] transition is thermalized and emits at nearly the maximum emission per C^+ ion (Tielens & Hollenbach 1985). The OH65 transition is pumped through absorption of far-IR photons and it is thus not sensitive to n_H and T_{gas} (G-A08). (5) $\Delta V = 100$ km s^{-1} in all models, describing the velocity dispersion along a characteristic line of sight. This has no effect in case of optically thin lines. As we show below, however, high columns and thus many overlapping (shadowing) regions characterize the environments where the OH65 absorption is produced, most likely forming a medium bound to the total potential of the galaxy center (Downes et al. 1993; Solomon et al. 1997). High ΔV is thus used to simulate the velocity dispersion due to random cloud-cloud motions, non-rigid rotation, and high-scale turbulence.

The above prescription leaves only two free parameters, T_{dust} and τ_{100}, the properties of the far-IR emission from which the observables W_{eq}(OH65), [C II]/FIR, L_{FIR}/M_{H2}, $f25/f60$, and $f60/f100$ are calculated. Figure 6 overlays the single-component model results (gray symbols and lines) and the data. Dashed gray lines connect model results for fixed T_{dust}, and solid gray lines connect model results for given τ_{100}. While the [C II] deficit is only a function of T_{dust} (dashed lines are nearly vertical in Figure 6(a)), W_{eq}(OH65) is sensitive to both T_{dust} and τ_{100}. Since our adopted OH and C^+ abundances are probably upper limits, Figure 6(a) indicates that moderately high $T_{dust} \gtrsim 50$ K and high column densities ($\tau_{100} \gtrsim 0.5$ or $N_H \gtrsim 6 \times 10^{23}$ cm^{-2}) are the lower limits that characterize objects with W_{eq}(OH65) $\gtrsim 20$ km s^{-1}. This is consistent with model results in Figure 6(b), where the L_{FIR}/M_{H2} values for these sources are reproduced with similar physical conditions.

For low τ_{100}, W_{eq}(OH65) increases supralinearly with τ_{100} (Figure 6) as a result of both the increasing strength of the

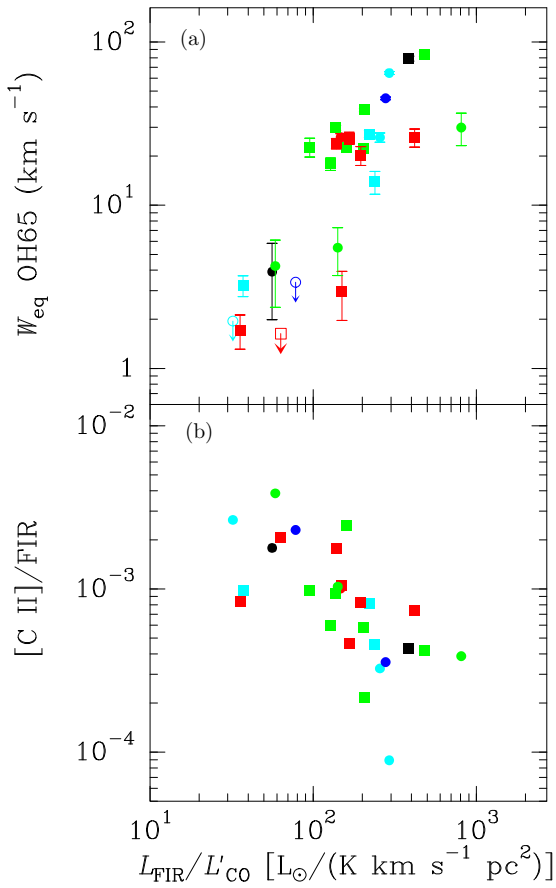

Figure 5. (a) Equivalent width of the OH65 transition between −200 and +200 km s^{-1} around the blue component of the doublet, and (b) the [C II]158 μm line to FIR ratio, as a function of the far-IR to CO (1–0) luminosity ratio in our galaxy sample. Symbol colors and shapes have the same meaning as in Figure 4.

radiation field that pumps the lower level of the transition, and the increasing OH column. However, the OH65 absorption saturates when the far-IR continuum approaches the optically thick regime ($\tau_{100} > 0.5$), as the far-IR field also saturates and only the externalmost shells of the source contribute to the absorption. The location of the data points in Figures 6(a) and (b) suggests that this optically thick regime for both the continuum and the OH65 transition applies to the majority of sources with W_{eq}(OH65) $\gtrsim$ 20 km s^{-1}. In contrast, sources like the prototypical starbursts M 82 and NGC 253, the H II galaxy UGC 5101, and the AGNs NGC 1068 and NGC 6240 have not developed these optically thick, prominent far-IR emitting structures,[21] though some of them may contain an embryo.[22]

The deficit in [C II] is produced because the cooling line cannot track the increase of $T_{dust}(G_0)$ (e.g., Kaufman et al. 1999). The region where carbon is ionized, and thus the total number of emitting C^+ ions, is restricted to $\tau_{FUV} \sim 1$ regardless of G_0, but the increase of G_0 increases the FIR continuum -thus lowering [C II]/FIR. Nevertheless, the presence of a [C II] deficit is not critically sensitive to the physical details of the PDRs and can be mostly understood in terms of the global L_{FIR}/M_{H2}: a strong upper limit on the [C II] emission is given by (G-A08)

$$\frac{L_{[C\,II]}}{L_{FIR}} < 8.3\times10^{-4}\times\left(\frac{X_{C^+}}{4\times10^{-5}}\right)\times\left(\frac{300\,L_\odot/M_\odot}{L_{FIR}/M_{H2}}\right), \quad (1)$$

which assumes optically thin [C II] emission with $T_{ex} \gg E_{upper} = 91$ K and up to 1/3 of all carbon ionized (for solar metallicities), which is high for molecular regions. In the optically thick regime, line saturation and extinction effects maintain a low [C II]/FIR even in case of high M_{H2}. Equation (1) directly links the [C II]/FIR ratio with L_{FIR}/M_{H2}, and shows that strong [C II] deficits are unavoidable in galaxies with high L_{FIR}/M_{H2}, i.e., those that are also strong in OH65 (Figures 6(a) and (b)).

The single component models, however, cannot account for the observed $f25/f60$ with the T_{dust} and τ_{100} inferred from the other panels of Figure 6. Indeed, the main consequence of assuming coexistent OH65 absorption and [C II] emission, i.e., modeling only one OH transition with a fixed covering factor of unity, is the underestimation of T_{dust} and τ_{100} (e.g., see multitransition, composite models for NGC 4418, Arp 220, and Mrk 231 in G-A12 and G-A14). Extended and optically thin regions of (U)LIRGs are emitters of both [C II] and 65 μm continuum (Díaz-Santos et al. 2014), and will dilute both the circumnuclear OH65 absorption and the [C II] deficit.

4.2. The OH71/OH65 Ratio and Composite Models

The ratio of the OH71 to the OH65 doublet absorption enables a better estimate of T_{dust} and τ_{100}, independent of the covering factor of the continuum by the excited OH. The modeled ratio of the total doublet equivalent widths, W_{eq}(OH71)/W_{eq}(OH65), is plotted as a function of T_{dust} (for $\tau_{100} \geqslant 0.4$) in Figure 7(a), and compared with the measured ratios. The observed minimum W_{eq}(OH71)/W_{eq}(OH65) $\gtrsim$ 0.2 ratio indicates $T_{dust} \geqslant 60$ K, significantly higher than inferred in Section 4.1. This lower limit is still very conservative for hot *sub*components in some sources, where higher-lying transitions of OH (at 53.0 and 56 μm) and H_2O indicate $T_{dust} \gtrsim 90$ K (G-A12; G-A14; N. Falstad et al., in preparation). In addition, unless the dust is very warm, the measured ratios in Figure 7(a) favor $\tau_{100} \gtrsim 0.7$, equivalent to $N_H \gtrsim 10^{24}$ cm^{-2}.

To account for the trends in Figure 4 together with the high T_{dust} inferred from W_{eq}(OH71)/W_{eq}(OH65) in many of the sources, we relax the assumptions in Section 4.1 and use composite models. It is assumed here that the bulk of the sources can be described by an optically thick very warm component (C_{thick}) that accounts for the OH65 absorption, and a colder, optically thin (presumably more extended) component (C_{thin}) that accounts for the bulk of the [C II] emission but gives negligible OH65 absorption. The physical conditions are: (1) C_{thick}: two models with $T_{dust} = 95$ and 60 K are considered (hereafter M_1 and M_2, respectively); in both, a nominal $\tau_{100} = 1$ is used. (2) C_{thin}: this is itself a model composed of two optically thin dust components with $T_{dust} = 65$ and 30 K, consistent with the G_0-range derived by Farrah et al. (2013) and with results independent of τ_{100} for values $\lesssim$0.1. The mix of these two components is governed by $\beta_{65-30} = L_{IR}^{65}/(L_{IR}^{65} + L_{IR}^{30})$, i.e., the fraction of the optically thin IR luminosity arising from the warm 65 K component, which is fixed to 0.75 and 0.25 for M_1 and M_2, respectively. The values of T_{dust} and β_{65-30} for C_{thin} are chosen to bracket the observed $f25/f60$ and $f60/f100$ colors for sources that have weak—but measurable—OH65 absorption. We adopt here a typical $n_H = 10^3$ cm^{-3} to simulate the [C II]

[21] The Compton-thick AGNs NGC 1068 and NGC 6240 (e.g., Burlon et al. 2011) are weak in OH65, probably because the X-ray absorber in these sources is too compact and hot to contribute significantly to the far-IR emission.
[22] In the deeply buried, edge-on starburst+AGN NGC 4945 (e.g., Spoon et al. 2000), there is most likely an optically thick far-IR emitting region, but either it is too cold to generate strong OH65 or the continuum emission from that component is highly diluted.

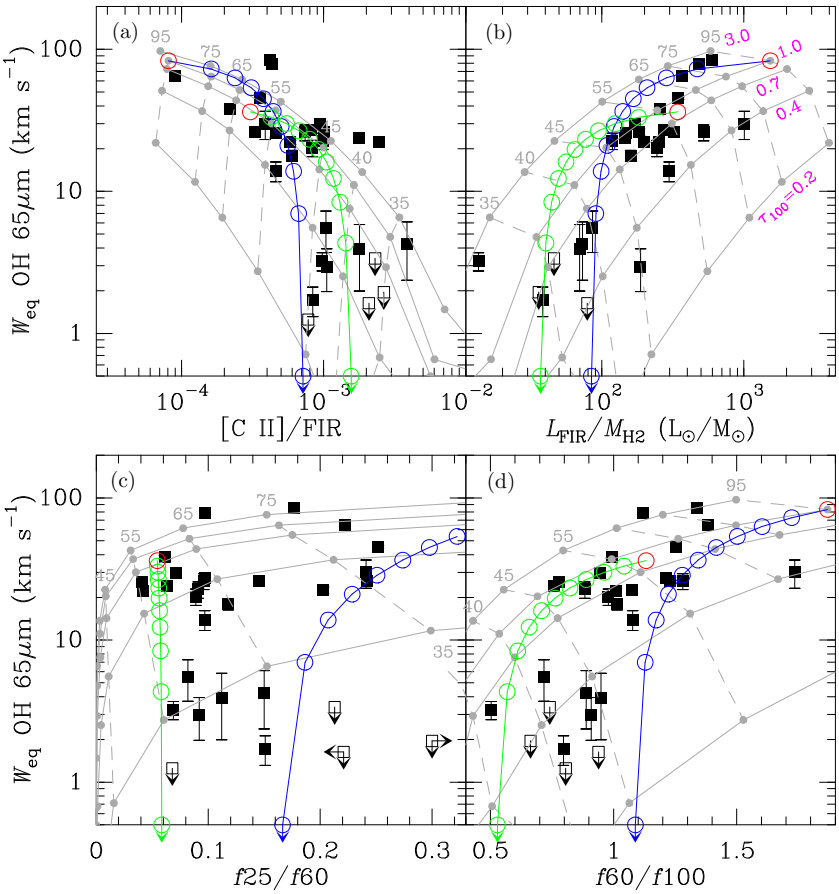

Figure 6. Same as Figure 4 with results from single-component (Section 4.1, gray symbols and lines) and composite (Section 4.2, blue and green) radiative transfer models overlaid. The single-component models are characterized by the dust temperature, T_{dust}, and the continuum optical depth at 100 μm, τ_{100}. Solid grey lines connect results with constant τ_{100} (indicated in magenta in panel (b)), and dashed grey lines connect results with constant T_{dust} (indicated with grey numbers, in K). The composite models have three components: two optically thin components with T_{dust} = 65 and 30 K, generating the bulk of the [C II] 158 μm emission but negligible OH 65 μm absorption, and one optically thick (τ_{100} = 1) and very warm (T_{dust} = 95 K for model M_1, blue symbols, and T_{dust} = 60 K for model M_2, green symbols) component, responsible for the OH 65 μm absorption. The mix of components is described by the parameters $\beta_{65-30} = L_{IR}^{65}/(L_{IR}^{65}+L_{IR}^{30})$ and $\beta_{thick} = L_{IR}^{thick}/L_{IR}^{total}$ (see Section 4.2). β_{65-30} = 0.75 and 0.25 for models M_1 and M_2, respectively. Along the sequence for both blue and green lines, β_{thick} is varied from 0 to 1 by intervals of 0.1, with β_{thick} = 1 indicated with a red circle.

emission (e.g., Malhotra et al. 2001; Parkin et al. 2013). The mix of C_{thick} and C_{thin} is described by the only free parameter $\beta_{thick} = L_{IR}^{thick}/L_{IR}^{total}$, the fraction of the total IR luminosity arising from the C_{thick} component.

Results for these models are shown in Figure 6; blue/green curves and circles correspond to models M_1/M_2, respectively. The circles on these curves represent a sequence of models where β_{thick} is varied from 0 to 1 in intervals of 0.1, with β_{thick} = 1 indicated with a red circle. According to this approach, the source position within the different observational planes is interpreted in terms of the overall energetic relevance of the optically thick, very warm structure (β_{thick}). For sources with W_{eq}(OH65) $\lesssim$ 6 km s^{-1}, $\beta_{thick} \lesssim$ 10%, while sources with W_{eq}(OH65) $\gtrsim$ 20 km s^{-1} are characterized by $\beta_{thick} \gtrsim$ 30%–50% for $M_1 - M_2$, respectively. In the latter objects, a fraction of the optically thin emission is expected to be reemission by dust heated by the optically thick component (Soifer et al. 1999; González-Alfonso et al. 2004), and thus C_{thick} most likely dominates the output of these galaxies. The modeled curves are consistent with the steep increase of W_{eq}(OH65) with decreasing [C II]/FIR below $\sim 10^{-3}$, and with increasing L_{FIR}/M_{H2} above $\approx$100 $L_\odot$/Msun. The [C II] emission is still underpredicted in some sources, which may suggest significant contributions by (diffuse) ionized gas.

5. CONCLUSIONS

Absorption in high-lying transitions of molecules with high dipolar moment and level spacing (i.e., mostly light hydrides), represented by OH65 and OH71, has been shown here to be strong in most local ULIRGs (79%) and in several LIRGs. Despite the high columns inferred in galaxies with high W_{eq}(OH), their low [C II]/FIR and low L'_{CO}/L_{FIR} suggest that both are associated with a "deficit" in M_{H2} relative to the far-IR continuum emission, accompanied by additional effects such as significant optical depth in the [C II] line and high excitation of CO. High columns and T_{dust} but low M_{H2}/L_{FIR} are indicative of high radiation densities and small volumes, with the high columns of gas and dust confined to small regions[23] around the bright, buried illuminating source(s) (nearly) dominating the galaxy output. The relationship between the model parameterization used here

[23] The effective size of the OH65 source can be determined by comparing the absolute L_{IR} (an upper limit of which is the observed luminosity) with its calculated value, $4\pi \int\int B_\nu(T_{dust})(1-\exp\{-\tau_\nu\})\,dS\,d\nu$, where dS stands for the projected surface and τ_ν is the continuum optical depth at frequency ν along the corresponding line of sight. For reference, the effective radius is $R_{eff} \approx 170$ pc for $L_{IR} = 10^{12}\,L_\odot$ ($R_{eff} \propto L_{IR}^{1/2}$), T_{dust} = 70 K, and τ_{100} = 1, which is a lower limit to the physical size in some galaxies owing to clumpiness. The diagnostics in Figure 4 and model results in Figure 6 are nevertheless independent of sizes and adopted distances.

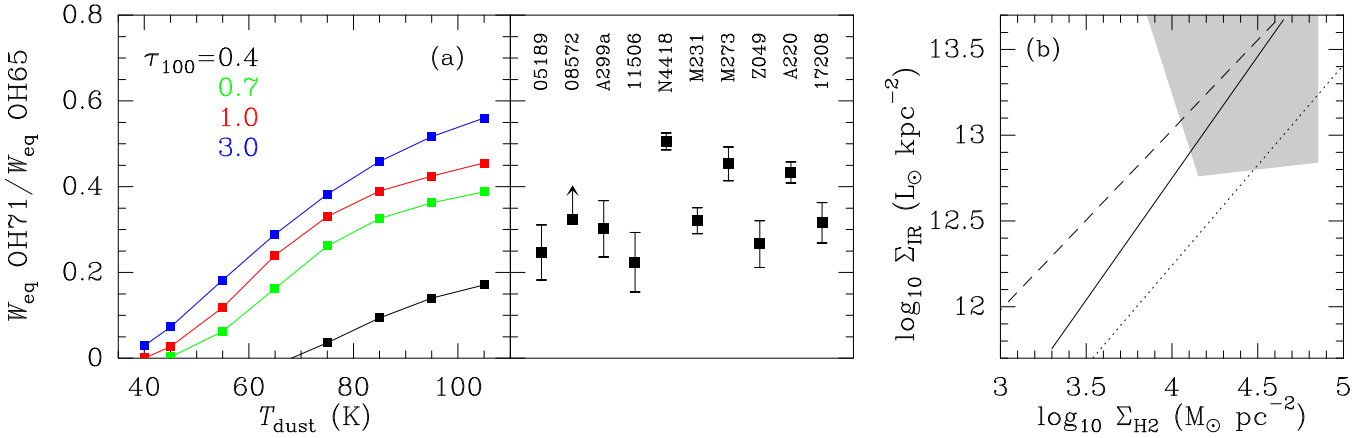

Figure 7. (a) Modeled W_{eq}(OH71)/W_{eq}(OH65) as a function of T_{dust} for $\tau_{100} \geqslant 0.4$, together with the ratios measured for the 10 sources where OH71 is detected, indicating $T_{dust} \gtrsim 60$ K. (b) Model-derived L_{IR} vs. H_2 mass in the surface density plane. The gray parallelogram identifies the region favored by the composite models (C_{thick}, Section 4.2) with $\tau_{100} = 0.5$–5 and $T_{dust} \geqslant 60$ K. Solid, dashed, and dotted lines show the fits to (U)LIRGs/mergers/SMGs given in Daddi et al. (2010), García-Burillo et al. (2012), and Genzel et al. (2010), respectively.

and that in terms of the dominant exciting source (AGN or starburst), volume and column densities, and ionization parameter (Abel et al. 2009; Fischer et al. 2014, G-C11), as well as the origin of the deficit in fine-structure lines other than [C II], will be explored in future work.

The inferred column densities associated with W_{eq}(OH65) $\gtrsim$ 20 km s^{-1}, $N_H \gtrsim 10^{24}$ cm^{-2}, are higher than those derived from the silicate strength at 9.7 μm. Models by Sirocky et al. (2008) indicate that the observed $\tau_{9.7} \lesssim 4$ can be explained with $\tau_V \lesssim 300$ ($N_H \lesssim 5 \times 10^{23}$ cm^{-2}). Since the OH65 regions/structure will block all the inner mid-IR emission passing through it, the observed mid-IR emission and associated silicate absorption are biased toward relatively unabsorbed mid-IR emitting regions. Likewise, several sources in the sample show mid-IR AGN signatures as [Ne V] emission (IRAS 05189-2524 and Mrk 273; Armus et al. 2007, V09) or an optical Broad Line Region (e.g., Mrk 231), and our direct view of this emission indicates tiny absorbing columns in comparison with those inferred from OH65. If the OH65 absorption is generated in a circumnuclear disk/torus/cocoon, either the combination of scale height/inclination, and/or clumpiness are required to account for the apparent decrease of extinction with decreasing wavelength. In sources with high contrast in mid-to-far infrared extinction, either extreme clumpiness or important inclination effects are necessarily involved. In other sources, extinction of the mid-IR emission by the OH65 structure is consistent with their low $f25/f60$ ratio. Though these structures are variably clumpy, the OH65 bimodality (Figures 1(b)–(c)) suggests that they are coherent and quickly formed, and provide an effective way to obscure the signposts of AGNs at shorter wavelengths in some sources.

In the direction of the warm, optically thick regions/structure where the OH65 absorption is produced, the surface density of both L_{IR} and H_2 mass are significantly higher than the average values previously estimated for the areas within the half-light radius (from CO or optical/UV). The grey parallelogram in Figure 7(b) indicates the location of the C_{thick} component for the ten sources where both OH65 and OH71 are detected: $\Sigma_{H2} \sim 10^{3.8}$–$10^{4.7}$ $M_\odot$ pc^{-2} ($\tau_{100} \sim 0.5$–5) and $\Sigma_{IR} \gtrsim 10^{12.8}$ $L_\odot$ kpc^{-2} ($T_{dust} \geqslant 60$ K). The latter high fluxes are consistent with previous estimates using sizes derived from radio emission and strengthen the role of radiation pressure support (Scoville 2004; Thompson et al. 2005, see their Figure 3). For starburst-dominated sources and using a Chabrier (2003) IMF, the corresponding SFRs are $\Sigma_{SFR} \gtrsim 10^{2.8}$ $M_\odot$ yr^{-1} kpc^{-2}. For hot *sub*components in some sources like the C_{core} component of NGC 4418, $\Sigma_{IR} \gtrsim 10^{14}$ $L_\odot$ kpc^{-2} and $\tau_{100} \gtrsim 8$ ($N_H \gtrsim 10^{25}$ cm^{-2}) on spatial scales of ≈20 pc (G-A12, Sakamoto et al. 2013; Costagliola et al. 2013; Varenius et al. 2014).

The solid, dashed, and dotted black lines in Figure 7(b) are extrapolations of the fits found in previous studies for subsamples of (U)LIRGs/mergers/SMGs. A pure SF scenario involves the shadowing of $\gtrsim$70 (for $\tau_{100} \gtrsim 1$) star-forming regions, each with $A_V \sim 10$ mag and $G_0 \gtrsim 10^4$, on spatial scales of a few × (10–100) pc; on spatial scales of a few parsecs, there is apparently no analog star-forming region close to the Galactic center.[24] The implied gas consumption timescales are $\tau_{gas} = (25\text{–}3.5) \times \tau_{100}$ Myr for $T_{dust} = 60$–95 K, comparable to those estimated for extreme sources exhibiting powerful OH outflows driven by buried AGNs (Sturm et al. 2011). On the other hand, 21 sources in our sample were analyzed in the OH 119 μm transition by V13, and 12 (9 with W_{eq}(OH65) > 10 km s^{-1}) were found to have $|v_{84}| \gtrsim 500$ km s^{-1} (the velocity below which 84% of the absorption takes place), most likely indicative of significant AGN feedback. The OH65-(U)LIRG phase may thus represent the starburst-AGN co-evolution phase in its shortlived most buried/active stage.

PACS has been developed by a consortium of institutes led by MPE (Germany) and including UVIE (Austria); KU Leuven, CSL, IMEC (Belgium); CEA, LAM (France); MPIA (Germany); INAFIFSI/OAA/OAP/OAT, LENS, SISSA (Italy); IAC (Spain). This development has been supported by the funding agencies BMVIT (Austria), ESA-PRODEX (Belgium), CEA/CNES (France), DLR (Germany), ASI/INAF (Italy), and CICYT/MCYT (Spain). E.G.-A. is a Research Associate at

[24] In Sgr B2(M), the peak of one of the most active and optically thick molecular cloud complexes in the Milky Way, W_{eq}(OH65) ≈ 2 km s^{-1} as measured with *ISO*/FP (Polehampton et al. 2007), consistent with its moderate effective $T_{dust} \sim 34$ K, $\Sigma_{IR} \sim 10^{11.8}$ $L_\odot$ kpc^{-2}, and $L_{FIR}/M_{H2} \sim 22$ $L_\odot/M_\odot$ for a gas-to-dust ratio by mass of 100 (Etxaluze et al. 2013). OH65 is not detected toward Sgr A* and its circumnuclear disk (Goicoechea et al. 2013), and is detected in emission toward the Orion bar PDR indicating collisional excitation in warm and dense gas (Goicoechea et al. 2011).

the Harvard-Smithsonian CfA, and thanks the Spanish Ministerio de Economía y Competitividad for support under projects AYA2010-21697-C05-0 and FIS2012-39162-C06-01. E.G.-A. and H.A.S. acknowledge partial support from NHSC/JPL RSA 1455432; H.A.S acknowledges NASA grant NNX14AJ61G. Basic research in IR astronomy at NRL is funded by the US-ONR; J.F. acknowledges support from NHSC/JPL subcontracts 139807 and 1456609. S.V. and M.M. acknowledge partial support from NHSC/JPL RSA 1427277 and 1454738. This research has made use of NASA's Astrophysics Data System and of GILDAS (http://www.iram.fr/IRAMFR/GILDAS).

Facility: Herschel (PACS)

REFERENCES

Aalto, S., Radford, S. J. E., Scoville, N. Z., & Sargent, A. I. 1997, ApJL, 475, L107
Abel, N. P., Dudley, C., Fischer, J., Satyapal, S., & van Hoof, P. A. M. 2009, ApJ, 701, 1147
Armus, L., Charmandaris, V., Bernard-Salas, J., et al. 2007, ApJ, 656, 148
Brauher, J. R., Dale, D. A., & Helou, G. 2008, ApJS, 178, 280
Burlon, D., Ajello, M., Greiner, J., et al. 2011, ApJ, 728, 58
Casoli, F., Willaime, M.-C., Viallefond, F., & Gerin, M. 1999, A&A, 346, 663
Chabrier, G. 2003, ApJL, 586, L133
Chung, A., Narayanan, G., Yun, M. S., Heyer, M., & Erickson, N. R. 2009, AJ, 138, 858
Costagliola, F., Aalto, S., Sakamoto, K., et al. 2013, A&A, 556, A66
Daddi, E., Elbaz, D., Walter, F., et al. 2010, ApJL, 714, L118
Díaz-Santos, T., Armus, L., Charmandaris, V., et al. 2013, ApJ, 774, 68
Díaz-Santos, T., Armus, L., Charmandaris, V., et al. 2014, ApJL, 788, L17
Downes, D., Solomon, P. M., & Radford, S. J. E. 1993, ApJL, 414, L13
Etxaluze, M., Goicoechea, J. R., Cernicharo, J., et al. 2013, A&A, 556, A137
Farrah, D., Lebouteiller, V., Spoon, H. W. W., et al. 2013, ApJ, 776, 38
Fischer, J., Abel, N. P., González-Alfonso, E., et al. 2014, ApJ, 795, 117
Fischer, J., Luhman, M. L., Satyapal, S., et al. 1999, Ap&SS, 266, 91
Fischer, J., Sturm, E., González-Alfonso,, et al. 2010, A&A, 518, L41
García-Burillo, S., Usero, A., Alonso-Herrero, A., et al. 2012, A&A, 539, A8
García-Marín, M., Colina, L., Arribas, S., Alonso-Herrero, A., & Mediavilla, E. 2006, ApJ, 650, 850
Genzel, R., Tacconi, L. J., Graciá-Carpio, J., et al. 2010, MNRAS, 407, 2091
Goicoechea, J. R., & Cernicharo, J. 2002, ApJL, 576, L77
Goicoechea, J. R., Etxaluze, M., Cernicharo, J., et al. 2013, ApJL, 769, L13
Goicoechea, J. R., Joblin, C., Contursi, A., et al. 2011, A&A, 530, L16
González-Alfonso, E., Fischer, J., Aalto, S., & Falstad, N. 2014a, A&A, 567, A91
González-Alfonso, E., Fischer, J., Bruderer, S., et al. 2013, A&A, 550, A25
González-Alfonso, E., Fischer, J., Graciá-Carpio, J., et al. 2012, A&A, 541, A4 (G-A12)
González-Alfonso, E., Fischer, J., Graciá-Carpio, J., et al. 2014b, A&A, 561, A27 (G-A14)
González-Alfonso, E., Smith, H. A., Ashby, M. L. N., et al. 2008, ApJ, 675, 303 (G-A08)
González-Alfonso, E., Smith, H. A., Fischer, J., & Cernicharo, J. 2004, ApJ, 613, 247
Goulding, A. D., Alexander, D. M., Bauer, F. E., et al. 2012, ApJ, 755, 5
Graciá-Carpio, J., Sturm, E., Hailey-Dunsheath, S., et al. 2011, ApJL, 728, L7 (G-C11)
Helou, G., Khan, I. R., Malek, L., & Boehmer, L. 1988, ApJS, 68, 151
Henkel, C., Whiteoak, J. B., & Mauersberger, R. 1994, A&A, 284, 17
Hollenbach, D. J., Takahashi, T., & Tielens, A. G. G. M. 1991, ApJ, 377, 192
Houghton, S., Whiteoak, J. B., Koribalski, B., et al. 1997, A&A, 335, 923
Kaufman, M. J., Wolfire, M. G., Hollenbach, D. J., & Luhman, M. L. 1999, ApJ, 527, 795
Kim, D.-C., Veilleux, S., & Sanders, D. B. 1998, ApJ, 508, 627
Luhman, M. L., Satyapal, S., Fischer, J., et al. 1998, ApJL, 504, L11
Luhman, M. L., Satyapal, S., Fischer, J., et al. 2003, ApJ, 594, 758
Malhotra, S., Kaufman, M. J., Hollenbach, D., et al. 2001, ApJ, 561, 766
Meijerink, R., Spaans, M., Loenen, A. F., & van der Werf, P. P. 2011, A&A, 525, A119
Mirabel, I. F., Booth, R. S., Johansson, L. E. B., Garay, G., & Sanders, D. B. 1990, A&A, 236, 327
Papadopoulos, P. P., van der Werf, P. P., Xilouris, E. M., et al. 2012, MNRAS, 426, 2601
Parkin, T. J., Wilson, C. D., Schirm, M. R. P., et al. 2013, ApJ, 776, 65
Pilbratt, G. L., Riedinger, J. R., Passvogel, T., et al. 2010, A&A, 518, L1
Poglitsch, A., Waelkens, C., Geis, N., et al. 2010, A&A, 518, L2
Polehampton, E. T., Baluteau, J.-P., Swinyard, B. M., et al. 2007, MNRAS, 377, 1122
Rupke, D. S., Veilleux, S, & Sanders, D. B. 2005, ApJS, 160, 87
Sakamoto, K., Aalto, S., Costagliola, F., et al. 2013, ApJ, 764, 42
Sanders, D. B., Mazzarella, J. M., Kim, D.-C., Surace, J. A., & Soifer, B. T. 2003, AJ, 126, 1607
Scoville, N. Z. 2004, in ASP Conf. Ser. 320, The Neutral ISM in Starburst Galaxies, ed. S. Aalto, S. Hüttemeister, & A. Pedlar (San Francisco, CA: ASP), 253
Scoville, N. Z., Young, J. S., & Lucy, L. B. 1983, ApJ, 270, 443
Sirocky, M. M., Levenson, N. A., Elitzur, M., Spoon, H. W. W., & Armus, L. 2008, ApJ, 678, 729
Soifer, B. T., Neugebauer, G., Matthews, K., et al. 1999, ApJ, 513, 207
Solomon, P. M., Downes, D., Radford, S. J. E., & Barrett, J. W. 1997, ApJ, 478, 144
Spoon, H. W. W., Farrah, D., Lebouteiller, V., et al. 2013, ApJ, 775, 127
Spoon, H. W. W., Koornneef, J., Moorwood, A. F. M., Lutz, D., & Tielens, A. G. G. M. 2000, A&A, 357, 898
Spoon, H. W. W., Marshall, J. A., Houck, J. R., et al. 2007, ApJL, 654, L49
Sturm, E., González-Alfonso, E., Veilleux, S., et al. 2011, ApJL, 733, L16
Surace, J. A., Sanders, D. B., & Mazzarella, J. M. 2004, AJ, 127, 3235
Thompson, T. A., Quataert, E., & Murray, N. 2005, ApJ, 630, 167
Tielens, A. G. G. M., & Hollenbach, D. 1985, ApJ, 291, 722
Varenius, E., Conway, J. E., Martí-Vidal, I., et al. 2014, A&A, 566, A15
Veilleux, S., Kim, D.-C., & Sanders, D. B. 1999, ApJ, 522, 113
Veilleux, S., Kim, D.-C., Sanders, D. B., Mazzarella, J. M., & Soifer, B. T. 1995, ApJS, 98, 171
Veilleux, S., Meléndez, M., Sturm, E., et al. 2013, ApJ, 776, 27 (V13)
Veilleux, S., Rupke, D. S. N., Kim, D.-C., et al. 2009, ApJS, 182, 628 (V09)
Véron-Cetty, M.-P., & Véron, P. 2006, A&A, 455, 773
Weiß, A., Walter, F., & Scoville, N. Z. 2005, A&A, 438, 533